nature geoscience

ARTICLES

https://doi.org/10.1038/s41561-020-0618-x

Valley formation on early Mars by subglacial and fluvial erosion

Anna Grau Galofre[1,2]✉, A. Mark Jellinek[1] and Gordon R. Osinski[3,4]

The southern highlands of Mars are dissected by hundreds of valley networks, which are evidence that water once sculpted the surface. Characterizing the mechanisms of valley incision may constrain early Mars climate and the search for ancient life. Previous interpretations of the geological record require precipitation and surface water runoff to form the valley networks, in contradiction with climate simulations that predict a cold, icy ancient Mars. Here we present a global comparative study of valley network morphometry, using a principal-component-based analysis with physical models of fluvial, groundwater sapping and glacial and subglacial erosion. We found that valley formation involved all these processes, but that subglacial and fluvial erosion are the predominant mechanisms. This is supported by predictions from models of steady-state erosion and geomorphological comparisons to terrestrial analogues. The inference of subglacial channels among the valley networks supports the presence of ice sheets that covered the southern highlands during the time of valley network emplacement.

Valley networks are ancient (3.9–3.5 billion years ago (Ga)) systems of tributaries with widely varying morphologies[1–4] predominately incised on the southern hemisphere highlands of Mars (Fig. 1). From comparisons with terrestrial rivers, many studies[4–10] interpreted their morphology in terms of erosion by surface runoff[4,5,9,11,12] and groundwater sapping[3,6,13], which requires the prolonged action of surface liquid water. However, the morphological variability of valley networks suggests that multiple erosional processes were at play. On Earth, water can erode through the action of surface runoff, but also by glacial processes and when confined in drainage channels beneath ice sheets. The development of Martian subglacial drainage conduits that lead to valley network incisions is appealing—it is in agreement with climate predictions of a Late Noachian Icy Highlands (LNIH)[14,15], and explains many puzzling morphologies that are inconsistent with erosion by surface runoff[1–4]. We therefore expand the current hypotheses for valley network formation to include subglacial erosion.

Here we examine the collective morphological statistics of valley networks and establish a quantitative classification scheme based on physical models of the four erosion processes introduced above. Our dataset includes 10,276 individual valleys[4], which comprise 66 valley networks (Fig. 1) characterized in terms of 6 landscape metrics tailored to capture distinctive fingerprints of fluvial, glacial, sapping and subglacial erosion[16,17]. We interrogated for common morphometries with a principal component analysis (PCA), understood with physical models of erosion. Our results characterize the morphological variability of Martian valley networks, and show that the morphometry of most valleys best corresponds to either fluvial or subglacial incision. We complement our analysis with a geomorphological comparison to terrestrial subglacial analogues.

Morphometry characterization and valley classification

We analysed 10,276 valley segments from a total of 59,423 mapped[4]. The selected systems (Fig. 1) span distinct incision time periods, provide a spatially meaningful coverage and reflect a variety of morphologies[2–4,9]. Our analysis employs six metrics: (1) junction angle between tributaries and main stem (γ), (2) streamline fractal dimension (D_f), (3) maximum network stream order (S_n), (4) width of first-order tributaries (λ), (5) length-to-width aspect ratio (R) and (6) magnitude of longitudinal profile reversals (undulations) (Ω) (refs [16,17]). The description of each parameter is summarized in Table 1.

We used the Mars Orbiter Laser Altimeter high-resolution stereo camera (MOLA/HRSC, 200 m per pixel) digital elevation model (DEM) as well as individual MOLA altimeter points to extract valley network longitudinal profiles and cross-sections, from which we measured the width and undulations (Supplementary Information). Stream order and length along the longest path were obtained from previous studies[4]. We measured the junction angle as the average of angles at all junctions, and extracted the streamline fractal dimension from MATLAB built-in algorithms (Methods and Supplementary Information).

Theoretical predictions for the steady-state form of the six metrics under fluvial, glacial, sapping or subglacial erosion regimes define synthetic valley networks (SVN), so that one SVN = (γ, D_f, S_n, λ, R, Ω). SVNs capture the range of values expected from each metric in each erosional regime (Methods and Supplementary Information), which enables the identification of the erosional mechanism that best explains valley network morphometry. Table 1 presents predictions for the average values of each metric and erosion style, so that each of the four columns on the right defines an average SVN. The mathematical models[16] and range of predictions are given in the Supplementary Information.

We explored valley network morphological variability first using a PCA to define distinct groups with common morphologies. Next, we understand the groups quantitatively with fluvial, glacial, sapping and subglacial steady-state SVNs. PCA enables a visualization of the six-dimensional dataset in two dimensions by presenting the data along the directions of maximum variance, the principal components (Methods and Supplementary Information). Valley networks group in the PCA space according to statistically common morphometries, whereas larger distances in the PCA indicate increasing

[1]Department of Earth, Ocean and Atmospheric Sciences, University of British Columbia, Vancouver, British Columbia, Canada. [2]School of Earth and Space Exploration, Arizona State University, Tempe, AZ, USA. [3]Department of Earth Sciences, University of Western Ontario, London, Ontario, Canada. [4]Institute for Earth and Space Exploration, University of Western Ontario, London, Ontario, Canada. ✉e-mail: agraugal@asu.edu

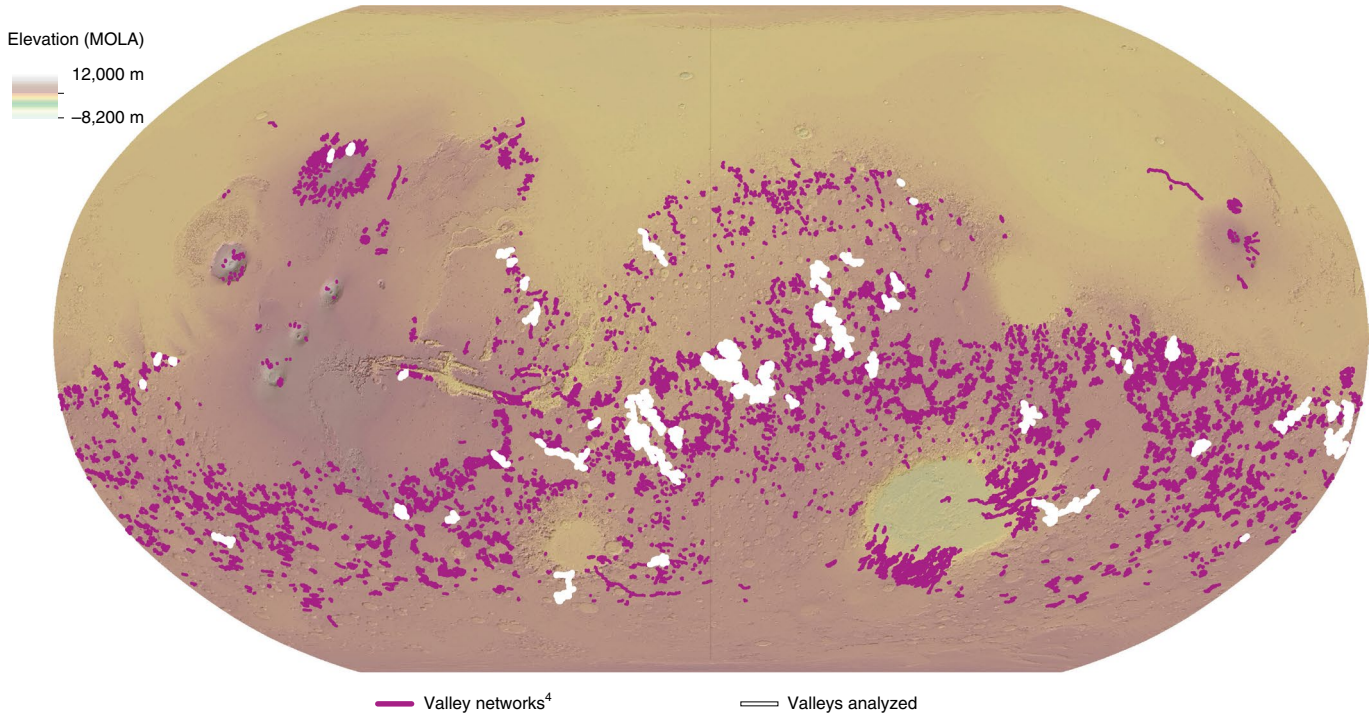

Fig. 1 | Distribution of analysed valley networks. Global map of Mars showing a blended MOLA/HRSC DEM overlain with valley network streamlines (purple). The systems analysed in this work are highlighted in white, and represent 10,276 individual valley systems of the 59,423 individual streamlines mapped[4], which belong to 66 valley networks.

Table 1 | Metric prediction averages

Metrics	Description	Fluvial	Glacial	Sapping	Subglacial
γ	Flow follows steady-state topography	60	90	72	60
D_f	Valley network streamline complexity	1.6	1.5	1.3	1.5
S_n	Tributary number, branching complexity	6	2	2	3
λ (m)	Initiation momentum balance	150	2,000	1,025	1,025
R	Basin-scale momentum balance	2,430	6	38	1,215
Ω (%)	Flow driven by pressure gradients	1	5	0.1	15

differences. To interpret the PCA beyond comparative statistics, we contrast valley network morphometry with a collection of 40,000 SVNs drawn from a Monte Carlo exploration of the Martian parameter space (Methods and Supplementary Information).

Figure 2 and Supplementary Table 3 show the PCA results, with valley network morphometries plotted against the first and second components, which captures 66% of the variance (Fig. 2a), and against the first and third components (Fig. 2b), which captures 57%. The relative contributions of each metric to the data variance (arrows in Fig. 2a,b insets) show the major controls on valley morphology. Martian valley networks are statistically less differentiated than terrestrial systems[16]: there are no distinct groups, but rather a continuum of morphologies.

To classify groups reliably, we used 10,000 SVNs drawn from Monte Carlo metric predictions. SVN groups define regions in the PCA (Fig. 2, shaded) that correspond to steady-state fluvial, glacial, sapping and subglacial morphometries. We evaluated the distance from each valley network to the 40,000 SVNs that make the four erosional groups, and attribute the origin of the system to the group of SVNs that minimizes this distance. A fifth group of statistically indistinct valleys is defined with the average morphology ($\langle VN \rangle \pm 2\sigma$) (Fig. 2, magenta), which forms the noise floor. Rivers and subglacial systems appear morphometrically similar, but differ in the presence of longitudinal profile undulations (Fig. 2b), which develop as a consequence of pressurized subglacial flow[17–22]. Valley networks with undulations $\Omega \geq 10\%$ are candidate subglacial channels, and were carefully analysed to discard post-emplacement profile disruptions (Supplementary Information). This is, importantly, the part of the analysis most susceptible of subjective interpretation (Supplementary Table 4).

We next evaluated the classification confidence (Fig. 2). If the distance from a valley network to the closest SVN group is much smaller than to any other, there is one clear origin (white dots). If the distance to two SVN groups is comparable to, but smaller than, the distance to the remaining groups, two possible processes explain the morphometry (light grey dots). Similarly, if the data permit three (dark grey) or all four (black) incision processes we classified accordingly (Supplementary Table 3).

Valley network distribution and large-scale glaciation. We identified 14 fluvial valley networks (Figs. 2 and 3), which include Samara, Warrego and Locras valles. They distribute along a trend of constant minimum width $\lambda \approx 100-300$ m, display negligible undulations $\Omega \approx 0$ and are characterized by the highest stream orders S_n and aspect ratios R in the dataset[16], which shows a high confidence.

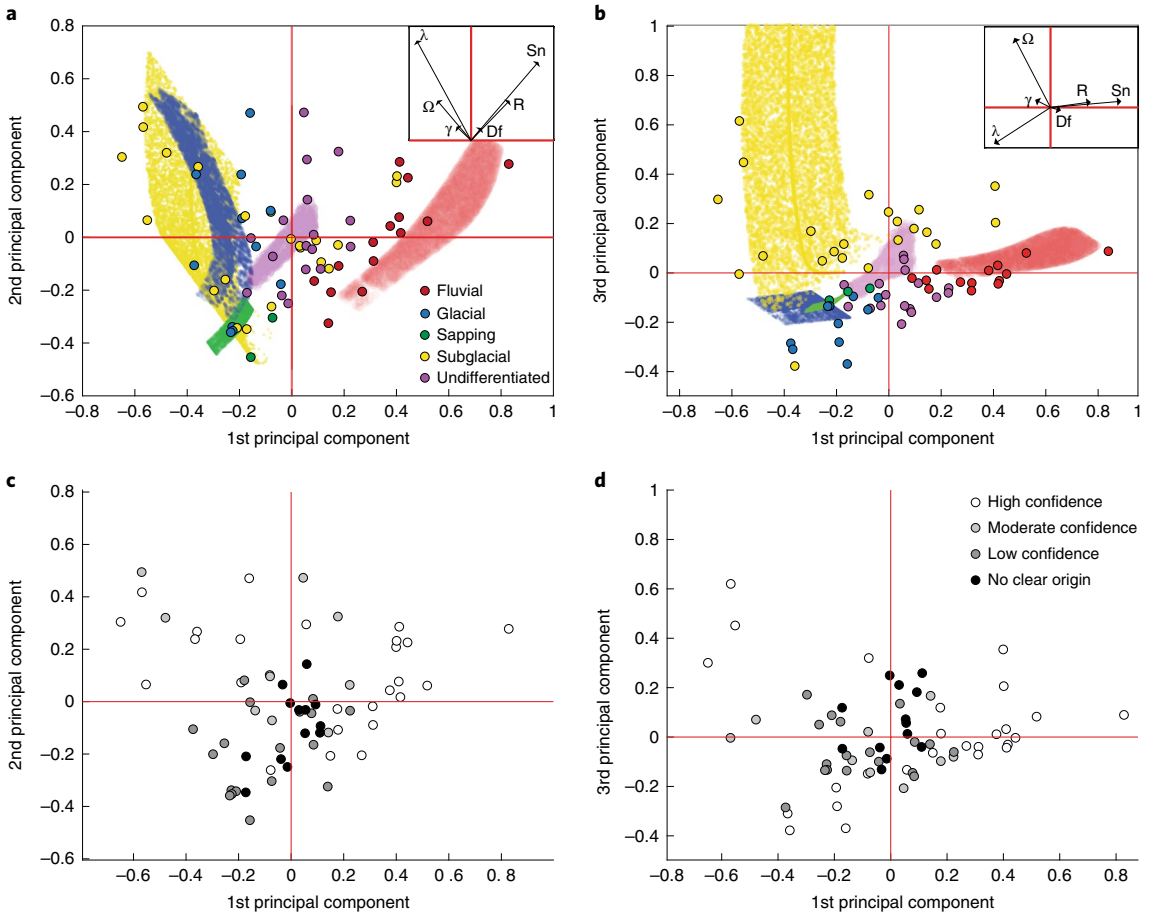

Fig. 2 | PCA classification and confidence. a,**b**, PCA analysis showing the valley networks (points) plotted in the first and second principal components (**a**) and first and third principal components (**b**), and colour-coded according to their inferred origin. Shaded regions correspond to Monte Carlo model predictions: fluvial (red), glacial (blue), subglacial (yellow), sapping (green) and undifferentiated (magenta). Insets: the six metrics with arrows scaled to the variance they capture. **c**,**d**, The characterization confidence: high confidence (white), moderate confidence (light grey), low confidence (dark grey) and no clear origin (black).

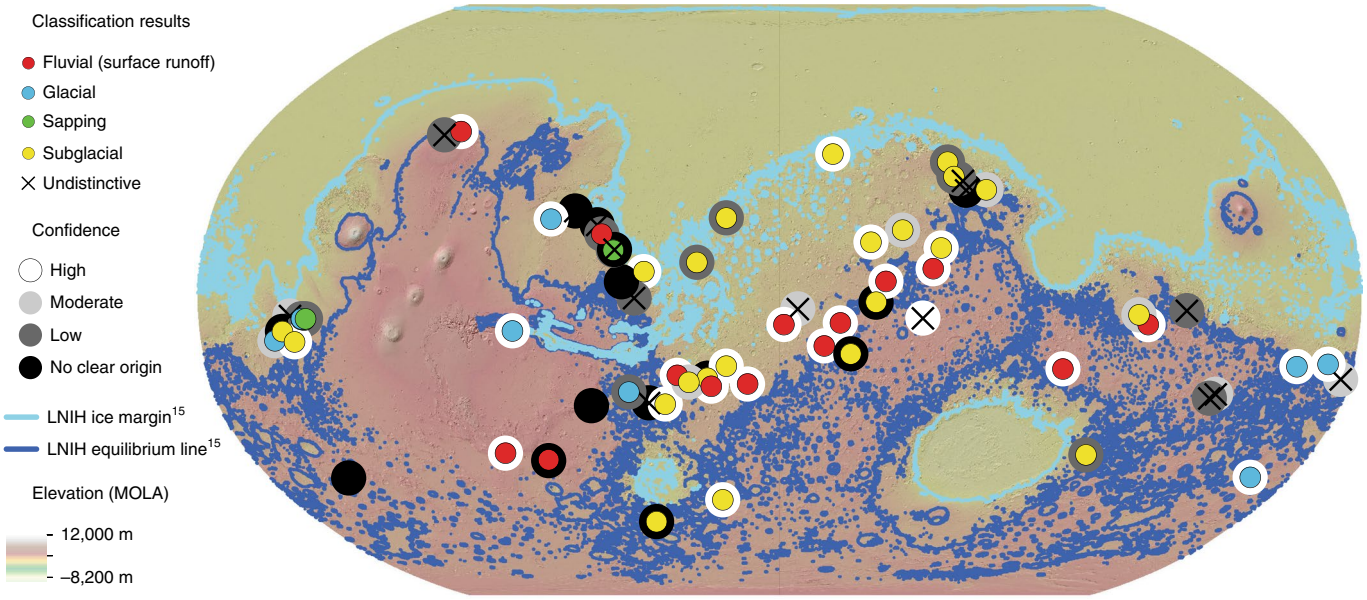

Fig. 3 | Valley network origin in the context of the Icy Highlands model. Global elevation map of Mars (blended MOLA/HRSC DEM at 200 m per pixel resolution; Methods) showcasing the valley network classification results and confidence values in the context of the ice terminus[15] (dark blue) and equilibrium[15] (light blue) lines for the LNIH scenario[14,15].

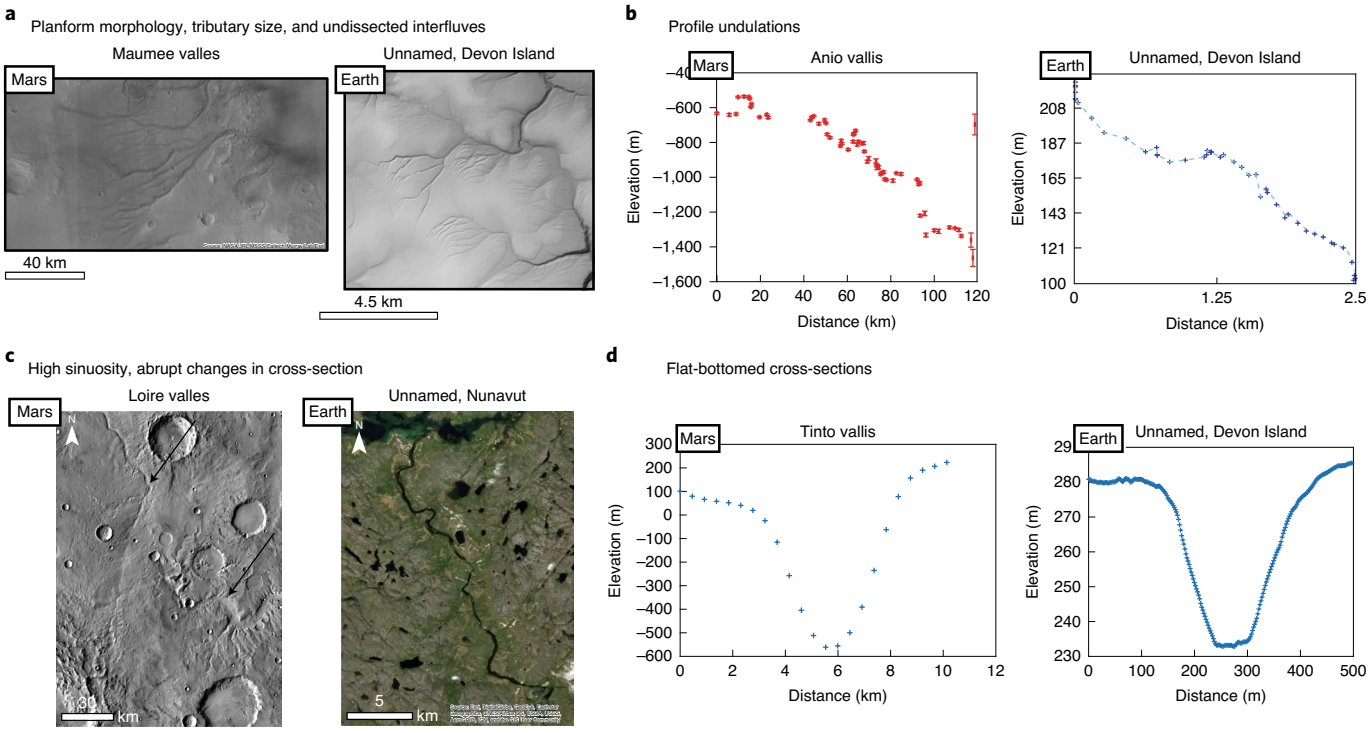

Fig. 4 | Comparative morphology of Martian and terrestrial subglacial systems. a, Planform morphology and lack of interfluve dissection. **b**, Longitudinal profiles with undulations above error bars for Anio Valles (MOLA altimetry) compared with a subglacial channel[17]. **c**, Comparison of cross-sectional variability and sinuosity (left, Thermal Emission Imaging System (THEMIS) mosaic (left) and right, satellite image (right). **d**, Trapezoidal cross-sections. Credit: Context Camera (CTX) mosaic, NASA/JPL/MSSS/Caltech Murray Lab/Esri (**a**, left); Arctic DEM hillshade, Polar Geospatial Center, University of Minnesota (**a**, right); THEMIS mosaic, ASU/NASA/USGS/Esri (**c**, left); Esri Maxar (**c**, right); blended MOLA/HRSC (**d**, left); Arctic DEM (**d**, right).

Spatially, they concentrate at the dichotomy boundary (Fig. 3). In contrast to glacial and subglacial systems, fluvial valleys require episodes of surface water stability on early Mars.

Erosion in subglacial channels best describes the morphology of 22 valley networks, shown with yellow dots in Fig. 3. Our identification of subglacial erosion on the basis of the PCA characterization as well as the presence of undulations (which do not always occur) provides a lower bound on the number of subglacial valley networks (Figs. 2 and 3).

Glacial erosion best explains nine valley networks (blue, Fig. 2), characterized by the largest minimum widths ($\lambda = 3-5$ km) and junction angles $\gamma \approx 90°$, distributed as shown in Fig. 3. Although seemingly scarce, retreating locally wet-based ice sheets often uncovers landscapes dissected by subglacial channels with no other apparent signs of glaciation, which includes valley glaciers (Fig. 4, Earth panels). Examples of these are found in Antarctica[19], and parts of the former Laurentide, Fennoscandian and Innuitian ice sheets[17,20,23–26].

Only three valley networks analysed are best explained with sapping erosion: small stream orders ($S_n = 1-2$), low aspect ratios ($R < 400$), and little junction angle variability $\gamma \approx 60$. The extent to which the data require a sapping origin is unclear based on our confidence analysis (Fig. 2), and probably subject to a better characterizations of substrate characteristics[12]. Sapping systems are generally located west of Tharsis (Fig. 3).

Finally, we identified 18 statistically indistinct systems (magenta dots in Fig. 2). Degradation over billions of years may have smoothed away characteristic morphometries to yield a shape close to the average valley network. These systems cannot be classified using our PCA. In contrast, valley networks with low confidence do not have a single clear origin (Methods and Supplementary Information). These valleys may: (1) reflect departures from steady-state erosional forms, (2) present characteristics consistent with overlapping processes or (3) reflect formation mechanisms not considered here.

Morphological evidence for subglacial incision

A comparison between terrestrial subglacial channels and Martian valley networks shows that common subglacial morphologies can explain several enigmatic valley network characteristics[3]. Figure 4 and Table 2 introduce these characteristics, which include planforms that displaying bifurcating (anabranching) branches, undissected interfluves and finger-like network patterns, wide first order tributaries that drain directly into the main stems[17,19,20,27], cross-sections that are steep-sided and flat-bottomed, mostly without visible inner channels, and that deepen but not widen down-valley[9,17]. Some of these characteristics have historically been attributed to sapping erosion[6,9,28]. However, subglacial channels produce similar morphologies[17,19,20] without the problems associated with sapping[12].

Terrestrial subglacial analogues (Fig. 4) and proposed Martian subglacial valleys display examples of these morphologies, and Table 2 shows examples of locations at which each of these characteristics are observed. In addition to undulations, the downstream invariance of valley width, large width of first-order tributaries and lack of intervalley dissection are hardly consistent with riverine erosion[17,29–31]. The large range in subglacial channel scales (kilometres[21] to centimetres[27], depending on substrate and discharge) can account for the scale differences between terrestrial and Martian systems.

Hydrology requirements for subglacial channel formation

A last piece of support for subglacial erosion comes from the spatial distribution of classified valley networks with respect to the models of a LNIH ice sheet[14,15,32]. Figure 3 shows that subglacial valley networks are mostly located between the equilibrium and terminus lines of a LNIH ice sheet, which would have involved five times the current

Table 2 | Morphological evidence for subglacial erosion

Observations	Observed on Earth	Observed on Mars
Qualitative		
Rare inner channels	High latitude[17,21]	Ubiquitous[2,46,47]
Invariant channel width	Devon Island[17]	Nanedi, VNs (22.2° S, 344.9° W)[2,3,6,48]
No metre-scale tributaries	Devon Island[17]	Ubiquitous[9,46,48]
Anabranching patterns	High latitude[17,19,20]	Loire, Evros, VNs (2° S, 243° W)[2,4,48]
Solitary channels	Alberta[49]	Reull and Surius Valles[3], this study
Rare alluvial fans	NY, Devon Island[17,50]	Ubiquitous[4]
Abrupt beginning and/or end	NY, Svalbard[50]	Nirgal Valles, VNs (3° S, 249° W)[3,48]
Intervalley undissected area	Devon Island[17,24]	Ubiquitous[3,4,46]
Drainage into main stem	Devon Island[17]	VNs (22.2° S, 344.9° W)[3,48,51]
Valley clustering	Devon Island[17]	Parana Valles region[3]
Wide range of scales	High latitude[21]	Ubiquitous (100 m to 10 km)[2,3]
Stepped long. profiles	High latitude[17,19]	Huygens Crater tributaries[4,47]
Trapezoidal cross-sections	Devon Island[17]	Ubiquitous (40° S to 40° N)[2]
Quantitative		
Large width-to-depth ratio	Devon Island[17]	Ubiquitous (40° S to 40° N)[2]
Undulating long profile	High latitude[17,20,21,50]	Ubiquitous[47], this study
Downslope oblique descent	High latitude[17,19,20,50]	Work in progress

VN, valley network.

surface water global equivalent layer (GEL)[15] (GEL 1-10x yields similar observations). Such a spatial distribution is consistent with theory[18,33] and observations[20,34] of subglacial channel origin: a meltwater-supply increase below the equilibrium line altitude combined with low sliding rates and enhanced basal pressure gradients drive subglacial channelization[33]. The number of subglacial channels sharply decreases above the equilibrium line altitude owing, for example, to a reduced meltwater supply[34] (Supplementary Fig. 1), consistent with Fig. 3.

In accord with predictions from ice-sheet modelling for the LNIH climate scenario[15,32], sustained basal ice melting and meltwater production occur with a water GEL of at least 10–15 times the current water inventory (34 m GEL, $\sim 5 \times 10^6$ km^3) (ref. [35]) and early geothermal heat flow rates of 55–65 mW m^{-2}. Although these are large water inventories for early Mars[36], localized basal meltwater accumulation does not require a sustained basal melting: moulins and crevasses deliver surface meltwater to the base of the ice (Greenland), internal friction due to basal shear can lead to basal melting (Antarctica) and localized volcanic activity can melt and channelize subglacial meltwater (Iceland)[37]. Taking into consideration the presence of subglacial channels, shortage of glacial valleys and the expected water inventories for early Mars, we hypothesize that a mostly cold-based ice sheet with localized basal melting is the most likely scenario. Terrestrial analogues are the Devon, Stacie and Müller polar caps.

Localized meltwater beneath a LNIH ice sheet can trigger subglacial valley network incision without the challenges related to rainfall and aquifer replenishment that erosion by surface runoff presents[38–41]. Basal meltwater accumulation under Martian ice sheets occurred under the Dorsa Argentea formation[42–44], arguably under a northern lowland glaciation[22], and could be occurring even in current conditions[45].

A morphological case for a glaciated early Mars

Understanding the origins of the Martian valley networks provides critical constraints on the climate and hydrosphere of early Mars. Here we depart from the common approach to studying individual valley networks to present a global statistical picture of the variability in valley morphometry, as well as a physical interpretation of their origin. Our PCA, understood with predictions drawn from erosion models (Fig. 2), distinguishes contributions from fluvial, glacial, sapping and subglacial incision, and shows that a majority of valley networks are a result of combined surface and subglacial runoff. Whereas fluvial valleys are localized draping around Arabia Terra, subglacial valley networks are widespread. Substantial morphological analogies with terrestrial subglacial channels (Fig. 4) complement the statistical and physical arguments and support the presence of subglacial erosion on Mars. This picture alters the current understanding that all Martian valley networks originated by surface runoff and provides geomorphological support for the presence of ice sheets on early Mars, which reconciles climate predictions with observations from the geological record.

Online content

Any methods, additional references, Nature Research reporting summaries, source data, extended data, supplementary information, acknowledgements, peer review information; details of author contributions and competing interests; and statements of data and code availability are available at https://doi.org/10.1038/s41561-020-0618-x.

Received: 14 November 2018; Accepted: 23 June 2020;
Published online: 03 August 2020

References

1. Carr, M. H. The Martian drainage system and the origin of valley networks and fretted channels. *J. Geophys. Res. Planet.* **100**, 7479–7507 (1995).
2. Williams, R. M. & Phillips, R. J. Morphometric measurements of Martian valley networks from Mars Orbiter Laser Altimeter (MOLA) data. *J. Geophys. Research Planet.* **106**, 23737–23751 (2001).
3. Gulick, V. C. Origin of the valley networks on Mars: a hydrological perspective. *Geomorphology* **37**, 241–268 (2001).

4. Hynek, B. M., Beach, M. & Hoke, M. R. Updated global map of Martian valley networks and implications for climate and hydrologic processes. *J. Geophys. Res. Planet.* **115**, E090008 (2010).
5. Carr, M. H. & Clow, G. D. Martian channels and valleys: their characteristics, distribution, and age. *Icarus* **48**, 91–117 (1981).
6. Laity, J. E. & Malin, M. C. Sapping processes and the development of theater-headed valley networks on the Colorado Plateau. *Geol. Soc. Am. Bull.* **96**, 203–217 (1985).
7. Kargel, J. S. & Strom, R. G. Ancient glaciation on Mars. *Geology* **20**, 3–7 (1992).
8. Lee, P. A Unique Mars/early Mars analog on Earth: the Haughton impact structure Devon Island, Canadian Arctic. In *Conference on Early Mars: Geologic and Hydrologic Evolution, Physical and Chemical Environments, and the Implications for Life* (eds Clifford, S. M., Treiman, A. H., Newsom, H. E. & Farmer, J. D.) 50 (LPI Contribution no. 916, Lunar and Planetary Institute, 1997).
9. Craddock, R. A. & Howard, A. D. The case for rainfall on a warm, wet early Mars. *J. Geophys. Res. Planet.* **107**, 5111 (2002).
10. Howard, A. D., Moore, J. M. & Irwin, R. P. An intense terminal epoch of widespread fluvial activity on early Mars: 1. Valley network incision and associated deposits. *J. Geophys. Res. Planet.* **110**, E12S14 (2005).
11. Baker, V. R., Carr, M. H., Gulick, V. C., Williams, C. R. & Marley, M. S. in *Mars* (eds Kieffer, H. H., Jakosky, B. M., Snyder, C. W. & Matthews, M. S.) 493–522 (Univ. Arizona Press, 1992).
12. Lamb, M. P. et al. Can springs cut canyons into rock? *J. Geophys. Res. Planet.* **111**, E07002 (2006).
13. Sharp, R. P. & Malin, M. C. Channels on Mars. *Geol. Soc. Am. Bull.* **86**, 593–609 (1975).
14. Wordsworth, R. et al. Global modelling of the early Martian climate under a denser CO_2 atmosphere: water cycle and ice evolution. *Icarus* **222**, 1–19 (2013).
15. Fastook, J. L. & Head, J. W. Glaciation in the Late Noachian Icy Highlands: ice accumulation, distribution, flow rates, basal melting, and top-down melting rates and patterns. *Planet. Space Sci.* **106**, 82–98 (2015).
16. Grau Galofre, A. & Jellinek, M. A. The geometry and complexity of spatial patterns of terrestrial channel networks: distinctive fingerprints of erosional regimes. *J. Geophys. Res. Earth Surf.* **122**, 1037–1059 (2017).
17. Grau Galofre, A., Jellinek, A. M., Osinski, G., Zanetti, M. & Kukko, A. Subglacial drainage patterns of Devon Island, Canada: detailed comparison of river and subglacial channels. *Cryosphere* **12**, 1461–1478 (2018).
18. Shreve, R. Movement of water in glaciers. *J. Glaciol.* **11**, 205–214 (1972).
19. Sugden, D. E., Denton, G. H. & Marchant, D. R. Subglacial meltwater channel systems and ice sheet overriding, Asgard Range, Antarctica. *Geogr. Annal. A* **73**, 109–121 (1991).
20. Greenwood, S. L., Clark, C. D. & Hughes, A. L. Formalising an inversion methodology for reconstructing ice-sheet retreat patterns from meltwater channels: application to the British Ice Sheet. *J. Quatern. Sci.* **22**, 637–645 (2007).
21. Kehew, A. E., Piotrowski, J. A. & Jørgensen, F. Tunnel valleys: concepts and controversies—a review. *Earth Sci. Rev.* **113**, 33–58 (2012).
22. Hobley, D. E., Howard, A. D. & Moore, J. M. Fresh shallow valleys in the Martian midlatitudes as features formed by meltwater flow beneath ice. *J. Geophys. Res. Planet.* **119**, 128–153 (2014).
23. Kleman, J. & Hättestrand, C. Frozen-bed Fennoscandian and Laurentide ice sheets during the Last Glacial Maximum. *Nature* **402**, 63–66 (1999).
24. Dyke, A. Last Glacial Maximum and deglaciation of Devon Island, Arctic Canada: support for an Innuitian Ice Sheet. *Quatern. Sci. Rev.* **18**, 393–420 (1999).
25. Hättestrand, C. & Stroeven, A. P. A relict landscape in the centre of Fennoscandian glaciation: geomorphological evidence of minimal Quaternary glacial erosion. *Geomorphology* **44**, 127–143 (2002).
26. England, J. et al. The Innuitian Ice Sheet: configuration, dynamics and chronology. *Quatern. Sci. Rev.* **25**, 689–703 (2006).
27. Walder, J. & Hallet, B. Geometry of former subglacial water channels and cavities. *J. Glaciol.* **23**, 335–346 (1979).
28. Malin, M. C. & Carr, M. H. Groundwater formation of Martian valleys. *Nature* **397**, 589–591 (1999).
29. Whipple, K. X. & Tucker, G. E. Dynamics of the stream-power river incision model: implications for height limits of mountain ranges, landscape response timescales, and research needs. *J. Geophys. Res. Solid Earth* **104**, 17661–17674 (1999).
30. Parker, G., Wilcock, P. R., Paola, C., Dietrich, W. E. & Pitlick, J. Physical basis for quasi-universal relations describing bankfull hydraulic geometry of single-thread gravel bed rivers. *J. Geophys. Res. Earth Surface* **112**, F04005 (2007).
31. Perron, J. T., Dietrich, W. E. & Kirchner, J. W. Controls on the spacing of first-order valleys. *J. Geophys. Res. Earth Surface* **113**, F04016 (2008).
32. Wordsworth, R. D., Kerber, L., Pierrehumbert, R. T., Forget, F. & Head, J. W. Comparison of 'warm and wet' and 'cold and icy' scenarios for early Mars in a 3-D climate model. *J. Geophys. Res. Planet.* **120**, 1201–1219 (2015).
33. Schoof, C. Ice-sheet acceleration driven by melt supply variability. *Nature* **468**, 803–806 (2010).
34. Rennermalm, A. K. et al. Understanding Greenland ice sheet hydrology using an integrated multi-scale approach. *Environ. Res. Lett.* **8**, 015017 (2013).
35. Christensen, P. R. Water at the poles and in permafrost regions of Mars. *Elements* **2**, 151–155 (2006).
36. Carr, M. & Head, J. Martian surface/near-surface water inventory: sources, sinks, and changes with time. *Geophys. Res. Lett.* **42**, 726–732 (2015).
37. Cuffey, K. M. & Paterson, W. S. B. *The Physics of Glaciers* (Academic, 2010).
38. Clifford, S. M. A model for the hydrologic and climatic behavior of water on mars. *J. Geophys. Res. Planet.* **98**, 10973–11016 (1993).
39. Wordsworth, R. D. The climate of early Mars. *Ann. Rev. Earth Planet. Sci.* **44**, 381–408 (2016).
40. Palumbo, A. M. & Head, J. W. Early Mars climate history: characterizing a 'warm and wet' Martian climate with a 3D global climate model and testing geological predictions. *Geophys. Res. Lett.* **45**, 10249–10258 (2018).
41. Rosenberg, E. N., Palumbo, A. M., Cassanelli, J. P., Head, J. W. & Weiss, D. K. The volume of water required to carve the Martian valley networks: improved constraints using updated methods. *Icarus* **317**, 379–387 (2019).
42. Head, J. W. & Pratt, S. Extensive Hesperian-aged south polar ice sheet on Mars: evidence for massive melting and retreat, and lateral flow and ponding of meltwater. *J. Geophys. Res. Planet.* **106**, 12275–12299 (2001).
43. Fastook, J. L., Head, J. W., Marchant, D. R., Forget, F. & Madeleine, J.-B. Early Mars climate near the Noachian–Hesperian boundary: Independent evidence for cold conditions from basal melting of the south polar ice sheet (Dorsa Argentea Formation) and implications for valley network formation. *Icarus* **219**, 25–40 (2012).
44. Butcher, F. E., Conway, S. J. & Arnold, N. S. Are the Dorsa Argentea on Mars eskers? *Icarus* **275**, 65–84 (2016).
45. Orosei, R. et al. Radar evidence of subglacial liquid water on Mars. *Science* **361**, 490–493 (2018).
46. Irwin, R. P., Howard, A. D., Craddock, R. A. & Moore, J. M. An intense terminal epoch of widespread fluvial activity on early Mars: 2. Increased runoff and paleolake development. *J. Geophys. Res. Planet.* **110**, E12S15 (2005).
47. Ansan, V., Mangold, N., Masson, P., Gailhardis, E. & Neukum, G. Topography of valley networks on Mars from Mars Express High Resolution Stereo Camera digital elevation models. *J. Geophys. Res. Planet.* **113**, E07006 (2008).
48. Carr, M. H. & Malin, M. C. Meter-scale characteristics of Martian channels and valleys. *Icarus* **146**, 366–386 (2000).
49. Rains, R. B. et al. Subglacial tunnel channels, Porcupine Hills, Southwest Alberta, Canada. *Quatern. Int.* **90**, 57–65 (2002).
50. Sissons, J. A subglacial drainage system by the Tinto Hills, Lanarkshire. *Trans. Edin. Geol. Soc.* **18**, 175–193 (1961).
51. Pieri, D. C. Martian valleys—morphology, distribution, age, and origin. *Science* **210**, 895–897 (1980).

Methods

Datasets. Our analysis requires topography and imagery data, as well as a high-resolution and manually mapped inventory of valley network streamlines. We used the blended MOLA/HRSC gridded topographic map with an equatorial resolution of 200 m per pixel (Supplementary Information). Given the importance of the correct identification of profile undulations, we analysed longitudinal profiles directly from individual MOLA laser altimeter points, acquired within 100 m of the streamlines, which accounts for the laser-pulse ground footprint of 100 m (ref. [52]), and filtered to correct for spikes and interpolation issues (Supplementary Section 2). We used CTX mosaics (12 m per pixel) for all the measurements that required high-resolution as well as to perform detailed observations of the location of each individual profile reversal. The complete dataset with a list of valley networks, morphometric measurements and their associated error is given in Supplementary Table 1. We used global CTX and THEMIS mosaics, overlain with MOLA coloured elevation data, to manually trace the main stem streamline used for longitudinal profile characterization, carefully following the valley bottom, whereas for the characterization of the whole network for stream order and junction angle purposes, we used the lines by Hynek et al.[4].

Measurement strategy. The junction angle is a statistical measure of the acute angle between tributary streamlines[4], averaged over all junctions in the valley network. Supplementary Fig. 2a exemplifies locations at which we took this measurement. Each measurement consists of the definition of a buffering distance of 1 km from the junction: larger distances introduce errors related to tributary sinuosity, and shorter distances may lead to resolution-related error. We clipped the tributary and main stem streamlines to the buffering distance, and extracted the beginning and end coordinates of each merging line. We then used the dot product of the vectors defined by both merging lines to extract each angle in the network.

The stream order S_n corresponds to the highest Strahler number in the network[53]. We obtained S_n directly from the valley network streamlines[4]. The same dataset[4] includes valley lengths along the longest path. A workflow of the process is shown in Supplementary Fig. 2b,c (length, L, and S_n, respectively).

To measure the valley network top width, we extracted ten cross-sectional curvature profiles on the highest stream order valleys in each network (Supplement. Fig. 2e), which we then combined to extract an average profile. We measured the valley network top width[2] as the mean distance between the points of maximum convexity in the average profile. The error of this measurement is evaluated in Supplementary Section 4. We then calculated the valley network aspect ratio R from the length L and this width W.

We obtained the width of order 1 tributaries λ by similarly measuring the top width (averaged over five profiles) over a statistical number of first-order tributaries (mor than ten if possible). Where the topographical resolution was not sufficient, we measured λ directly from the CTX imagery (Supplementary Fig. 2f). The error of this measurement is described in Supplement Section 4.

From the longitudinal profile data (Supplementary Fig. 2d), we quantified Ω as the elevation difference between the local minima at the beginning of a positive topographic gradient section, h_{min}, and the following local maxima, h_{max}, to the total topographic loss ΔH: $\Omega = (h_{max} - h_{min})/\Delta H$. As detailed above and in Supplementary Section 2, longitudinal profiles were extracted from laser altimeter points, filtered and visually evaluated to account for (1) stitching errors, (2) large interpolated sections and (3) post-emplacement surface modification: craters and ejecta infill, folding, faulting, chaos and subsidence, and sedimentary infill from tributaries and so on. We used CTX mosaic observations, reported in Supplementary Table 4, to spatially identify these features on the longitudinal profiles and remove their contributions to the undulations measurement (Supplementary Figs. 4 and 5). More details and case studies are given in Supplementary Section 2.1.

Details of the PCA technique. Multivariate statistics and machine learning, such as self-organizing maps, have been used to classify valley networks[54,55], albeit without a quantitative interpretation of the classification results in terms of morphology. Here we used a PCA algorithm followed by the interpretation of the classification results in terms of physical models. The PCA technique is a multidimensional linear statistical analysis that uses an eigenvalue decomposition of the data covariance matrix to define a new, orthogonal basis set of linearly independent vectors called principal components. By definition of the transformation, the first principal component captures the largest variance, and each succeeding component captures a progressively smaller fraction. In our valley network database, the first three principal components capture ~82% of the total variance and are considered sufficient for our characterization. Supplementary Section 3 includes more technical details of the PCA technique and PCA error bar propagation, and analyses the influence of sample size on our results.

Metric predictions. The interpretation of the PCA relies on calculating the distance between the SVNs that result from the physical models[16,17] (Supplementary Information) and the data point represented by each valley network analysed. Shaded areas in Fig. 2 correspond to the model predictions, each encompassing 10,000 SVN, which correspond to steady-state fluvial, glacial, subglacial and sapping processes. Each SVN within is calculated using different combinations of parameters (Supplementary Table 2).

The mathematical models that describe each metric are given in Supplementary Section 6. Some metrics, notably the stream order and minimum width, do not yet have supporting physical models. To reduce the effect on the predictions of those metrics, we instead used the statistical average value, which tends to move the SVN predictions towards the origin of the coordinates and minimize the effect on the variance.

Upper and lower reasonable parameter bounds for Mars, compiled in Supplementary Table 2, define the parameter space for our models. Using a Monte Carlo method, we randomly selected 10,000 combinations of parameters to derive values for each of the metrics, so that each unique combination was used to produce one SVN. Table 1 presents the average metric predictions and the meaning of each metric, whereas the parameter ranges and upper/lower bounds are given in Supplementary Table 2.

The resulting 40,000 SVNs were then projected in the principal component space and colour coded (Fig. 2) according to the mechanism of erosion considered. The origin of each valley network, as well as the confidence, was assessed in terms of the distance to the four groups of SVNs that represent the steady-state form of each erosional process. Valley networks that overlap the shaded spaces are consistent with the steady-state form of that erosional process. However, caution and a careful calculation is necessary to interpret the results of Fig. 2, as it represents a two-dimensional projection of a six-dimensional space and the relative distances may appear distorted.

Supplementary Information, in particular Supplementary Sections 2–6, contains detailed workflows and additional details of the measurement, error evaluation and classification process.

Data availability

Datasets generated during the current study, which include observations, model parameters and longitudinal profile data have been deposited in the Zenodo repository at https://zenodo.org/record/3890557#.XwgnIigzaUl and are included in this article as Supplementary tables.

Code availability

Data analysis codes include the PCA (available as the MATLAB built-in function pca) as well as custom codes specifically generated for data and error extraction, error propagation, confidence analysis and modelling of the synthetic fluvial, glacial, sapping and subglacial valley networks. The authors will provide the custom codes in a MATLAB live script format (.mlx) upon request.

References

52. Smith, D. E. et al. Mars Orbiter Laser Altimeter: experiment summary after the first year of global mapping of Mars. *J. Geophys. Res. Planet.* **106**, 23689–23722 (2001).
53. Horton, R. E. Erosional development of streams and their drainage basins; hydrophysical approach to quantitative morphology. *Geol. Soc. Am. Bull.* **56**, 275–370 (1945).
54. Stepinski, T. & Stepinski, A. Morphology of drainage basins as an indicator of climate on early Mars. *J. Geophys. Res. Planet.* **110**, E12S12 (2005).
55. Bue, B. D. & Stepinski, T. F. Automated classification of landforms on Mars. *Computat. Geosci.* **32**, 604–614 (2006).

Acknowledgements

A.G.G., A.M.J. and G.R.O. were supported through the NSERC Discovery grant program. A.G.G. also received support through an NSERC CREATE-funded fellowship and through an Exploration Fellowship from the School of Earth and Space Exploration, ASU. Arctic fieldwork was supported through PCSP and NSERC Northern Research Supplement Grants to G.R.O. Our appreciation goes to C. Schoof, R. Phillips, K. Whipple and P. Christensen for their insightful comments, and to the MJ-CJ research group for continued support.

Author contributions

A.G.G. and A.M.J conceived the study. A.G.G. carried out all the calculations, performed the data analysis summarized in Figs. 2–4 and took the lead in writing the paper with A.M.J. G.O. provided critical comments related particularly to geological controls on the history of Mars surface processes. All the authors contributed to constructing the discussion and implications for Mars' hydrosphere and early climate.

Competing interests

The authors declare no competing interests.

Additional information

Supplementary information is available for this paper at https://doi.org/10.1038/s41561-020-0618-x.

Correspondence and requests for materials should be addressed to A.G.

Peer review information Primary handling editor: Stefan Lachowycz.

Reprints and permissions information is available at www.nature.com/reprints.

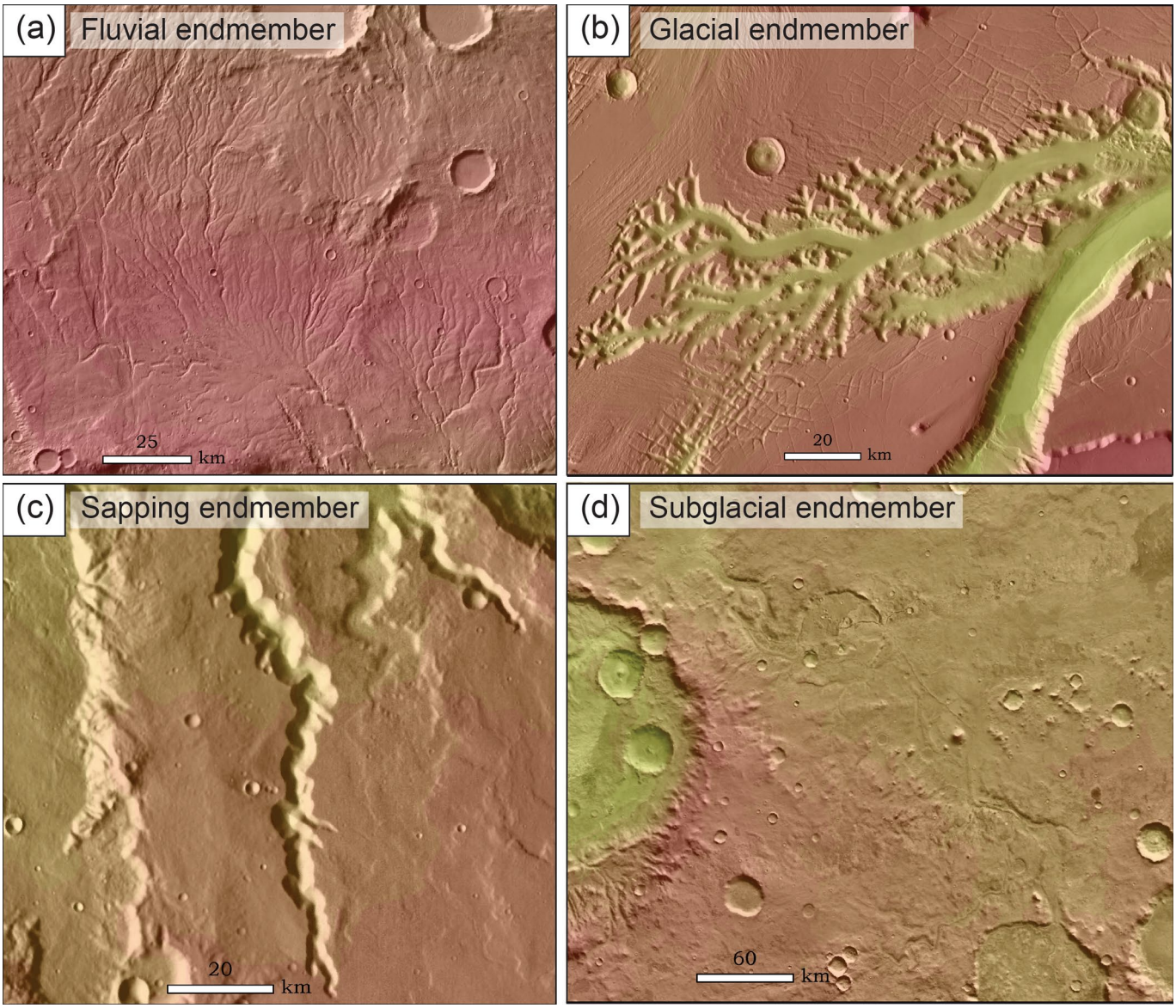

Extended Data Fig. 1 | PCA endmember examples. Examples of the four groups of valley networks as derived from the PCA classification: Warrego valles, fluvial (**a**), unnamed valley (M68), glacial (**b**), Abus vallis, sapping (**c**), and Pallacopas valles, subglacial (**d**). Images show colorized elevation (MOLA, Goddard Space Flight Center) overlying a THEMIS (ASU/NASA) mosaic.